Conductive Co-based metal organic framework nanostructures for excellent potassium- and lithium-ion storage

Kinetics and mechanism studies

Mao, Pengcheng ; Fan, Huilin ; Liu, Chang ; Lan, Gongxu ; Huang, Wei; Li, Zhipeng ; Mahmoud, Hitham; Zheng, Runguo ; Wang, Zhiyuan ; Sun, Hongyu

DOI
10.1039/d2se00520d

Publication date
2022

Document Version
Final published version

Published in
Sustainable Energy and Fuels

Sustainable Energy & Fuels

ROYAL SOCIETY OF CHEMISTRY

PAPER

View Article Online
View Journal | View Issue

Cite this: *Sustainable Energy Fuels*, 2022, **6**, 4075

Conductive Co-based metal organic framework nanostructures for excellent potassium- and lithium-ion storage: kinetics and mechanism studies†

Pengcheng Mao,[a] Huilin Fan,[a] Chang Liu,[a] Gongxu Lan,[a] Wei Huang,[b] Zhipeng Li,*[c] Hitham Mahmoud,*[de] Runguo Zheng,[afg] Zhiyuan Wang,[afg] Hongyu Sun *[f] and Yanguo Liu*[afg]

Thanks to the low cost and earth's abundant potassium resources, potassium ion batteries (PIBs) have attracted much interest as alternative energy storage devices. However, there is still a great challenge to develop suitable anode materials for PIBs with high specific capacity, fast charge/discharge and stable ion storage. Nowadays, conductive metal–organic frameworks (c-MOFs) with excellent physicochemical properties are employed for different electrochemical applications, but the study of their potassium storage performance remains unknown, and the detailed potassium storage mechanism needs to be explored. Herein, nanostructured $Co_3(HHTP)_2$ c-MOF (Co-CAT MOF, HHTP: 2,3,6,7,10,11-hexahydroxytriphenylene) is synthesized by a liquid-phase method and evaluated as the anode for PIBs. The active sites and open pathways in the conductive Co-CAT MOF promote ion diffusion and electron transfer, exhibiting high reversible specific capacity (332 mA h g^{-1} at 0.1 A g^{-1}), excellent long-cycle stability (230 mA h g^{-1} at the current density of 1.0 A g^{-1} after 700 cycles) and outstanding rate performance (165 mA h g^{-1} at 4.0 A g^{-1}), which is superior to the typical PIB anodes. Combined with different *ex situ* characterization techniques, the potassium storage mechanism based on 8-electron transfer is revealed. Furthermore, Co-CAT MOF exhibits excellent Li-ion storage performance. In the half-cell, the Co-CAT MOF electrode displays a high reversible capacity of 800 mA h g^{-1} at 200 mA g^{-1}. In addition, the Co-CAT//$LiCoO_2$ full cell cycles for 100 cycles at 200 mA h g^{-1}. It is believed that Co-CAT MOF is a promising electrode material for potassium/lithium storage, and the proposed ion storage mechanism can be used to discover other MOF-based electrodes for energy storage.

Received 15th April 2022
Accepted 18th July 2022

DOI: 10.1039/d2se00520d

rsc.li/sustainable-energy

Introduction

Lithium-ion batteries (LIBs) have the advantages of high energy density and long service life, and thus have wide applications in mobile devices, electrical vehicles, and large-scale electric energy storage.[1–4] One main drawback of LIBs is the limited resources and the unbalanced distribution of lithium metal all over the world.[5,6] It is of great importance to develop other energy storage devices based on earth abundant elements. As an alternative, potassium ion batteries (PIBs) have attracted much attention in recent years.[7–9] One important reason is the abundance and low cost of potassium element in comparison with lithium, making PIBs a promising candidate for different applications.[6,10,11] Besides that, the device configuration and the fabrication procedures of PIBs are similar to those of LIBs, and there is no essential difference in the electrochemical ion storage in both devices.[12] It means the current knowledge and techniques for LIBs development (including anodes, cathodes, electrolytes, separators, *etc.*) can be transferred to PIBs.[13] The

[a]*School of Materials Science and Engineering, Northeastern University, Shenyang 110004, PR China. E-mail: lyg@neuq.edu.cn*

[b]*School of Chemistry and Materials Science, Hunan Agricultural University, Changsha 410128, PR China*

[c]*Beijing Advanced Innovation Center for Materials Genome Engineering, School of Materials Science and Engineering, University of Science and Technology Beijing, Beijing 100083, PR China. E-mail: zplmse@ustb.edu.cn*

[d]*Else Kooi Laboratory, Faculty of Electrical Engineering, Mathematics and Computer Science, Delft University of Technology, Feldmannweg 17, 2628 CT Delft, The Netherlands. E-mail: H.M.AminHassan@tudelft.nl*

[e]*Chemistry Department, Faculty of Science, Zagazig University, Alsharkia 44519, Egypt*

[f]*School of Resources and Materials, Northeastern University at Qinhuangdao, Qinhuangdao 066004, PR China. E-mail: hyltsun@gmail.com*

[g]*Key Laboratory of Dielectric and Electrolyte Functional Material Hebei Province, Northeastern University at Qinhuangdao, Qinhuangdao 066004, PR China*

† Electronic supplementary information (ESI) available. See https://doi.org/10.1039/d2se00520d

key difference lies in the size of the ionic radius. The potassium-ion radius (0.138 nm) is larger than that of lithium-ion (0.076 nm), resulting in a limited capacity, sluggish kinetics, and irreversible structural collapse of the electrode during potassiation/depotassiation.[5,14–18] It is significant to develop advanced electrodes for PIBs with high specific capacity, excellent rate performance and stability.

The typical anode materials for PIBs include carbon-based electrodes,[9,15,16,19] transition metal compounds,[20,21] MXene,[14,22,23] organic compounds,[24–26] *etc.* Among those materials, metal organic frameworks (MOFs) are promising anodes for potassium storage, thanks to their merits of low cost, low density, multiple redox sites, and abundant porosity.[12,27–30] Taking advantage of the sufficient inner space of MOFs, Li *et al.* demonstrated that a novel rectangular-shaped $[C_7H_3KNO_4]_n$ MOF can be used as the anode for efficient potassium storage,[26] which maintained a specific capacity of 123 mA h g^{-1} after 150 cycles at a current density of 50 mA g^{-1}. The abundant N–K/O–K coordination bonds through the MOF pores are responsible for the excellent electrochemical performance. It should be noted that the conventional MOFs that are synthesized using nonconjugated organic ligands usually show poor electronic conductivity and slow reaction kinetics.[31–34] Different strategies have been employed to solve the issues, such as combining the MOFs with other conductive agents (carbon nanotubes,[35] graphene,[36] conductive polymers,[37] *etc.*). The composite electrodes show better electrical conductivity and more efficient electron/ion migration. However, the conductive agent's addition decreases the effective volume density of MOFs as the main active materials.

The other strategy is to develop conductive MOFs (c-MOFs) with intrinsic high electronic conductivity.[31–34,38,39] In those materials, the charges are delocalized in the entire structure, which facilitates the charges' directional movement.[38,40] Combining the abundant porosity and redox active sites, c-MOFs show great potential for electrochemical energy storage.[31,33,41] For example, the extended graphene-like conjugated structure in Ni_3(2,3,6,7,10,11-hexaiminotriphenylene)$_2$ (Ni-MOF) facilitates the in-plane delocalization of charge and improves the electrical conductivity (σ = 1.8 S cm^{-1}). Meanwhile, the filamentous nanostructure exhibits a high specific surface area, which promotes charge transfer, electrolyte infiltration and ion migration.[33] The Ni-MOF electrode exhibited a reversible specific capacity of 362 mA h g^{-1} after 500 cycles at a high current density of 5 A g^{-1} for lithium storage, indicating the potential of Ni-MOF for practical applications. When a c-MOF is used as a PIB anode, its abundant pores can alleviate the volume change caused by the repeated potassiation and depotassiation.[42] However, the capacity exerted by c-MOFs during cycling is unsatisfactory, exhibiting capacity mostly less than 210 mA h g^{-1} especially under high current densities (Table S1†), which hinders further utilization of those materials for potassium storage. Moreover, the detailed potassiation/depotassiation kinetics and the ion storage mechanism of c-MOF based anodes are still unclear, making it even more challenging to optimize their electrochemical performance and design novel MOF-based electrodes for PIBs.

Herein, by using a facile solution phase method, we successfully synthesized a nanoscale $Co_3(HHTP)_2$ (Co-CAT MOF, HHTP = 2,3,6,7,10,11-hexahydroxytriphenylene) MOF, and studied the electrochemical potassium storage performance. The cross-linked porous network structure is conducive to ion/electron conduction, and has good mechanical properties, which shows a high ion diffusion coefficient. When evaluated as the anode for PIBs, the Co-CAT MOF electrode shows a specific capacity of 280 mA h g^{-1} at a current density of 500 mA g^{-1}. Even at a high current density of 1 A g^{-1}, the Co-CAT MOF electrode still maintains a reversible specific capacity of 230 mA h g^{-1} after 700 cycles. Combining electrochemical kinetic analysis with a series of *ex situ* characterization techniques, the origin of the excellent electrochemical performance and the ion storage mechanism of the Co-CAT MOF electrode were revealed. It was found that the C=C bonds in Co-CAT MOF are the active sites for reversible potassium storage, while Co nodes and other structures are electrochemically inert but keep the structure stable. Furthermore, both Li-ion half-cells and full-cells based on Co-CAT MOF electrodes exhibit excellent electrochemical performance. This work demonstrates the feasibility of Co-CAT MOF for PIB application, and reveals the potassium ion storage mechanism of such materials, which is significant for designing novel electrode materials for energy storage.

Results and discussion

The Co-CAT MOF materials were synthesized by using a simple liquid-phase bottom-up assembly strategy. During the reaction, cobalt ions undergo a coordination reaction with hydroxyl groups in HHTP, leading to an increased redox active sites and pore density in the entire system. The coordination expands along the *a*–*b* plane to form a two-dimensional π-conjugate expansion framework with a honeycomb pore structure (see Scheme S1†). At the same time, the entire plane is stacked along the *c*-axis to form a wire structure.[43–46]

The morphology and microstructure of the synthesized samples were studied by electron microscopy observations. As can be seen in Fig. 1A and B, the sample shows a cross-linked porous network morphology, which is formed by interconnected nanowires with random orientations. The average length and diameter of the nanowires are 500 nm and 50 nm, respectively, which are further confirmed by the TEM studies (Fig. 1C and D). The high-magnification SEM image (Fig. 1B inset) shows that the nanowire cross-sections have a regular hexagonal shape, which is consistent with the crystal structure of Co-CAT MOF along the [001] projection (Scheme S1†). From the high-resolution transmission electron microscopy (HRTEM) image (Fig. 1E), obvious lattice fringes can be resolved, and the lattice distance of 1.76 nm corresponds to the (100) plane of Co-CAT crystals.[45] The high-angle annular dark-field scanning transmission electron microscopy (HAADF-STEM) image (Fig. 1F) and the related energy dispersive X-ray mapping (Fig. 1G–I) prove that the sample contains C, O, and Co elements with a uniform distribution along the nanowire.

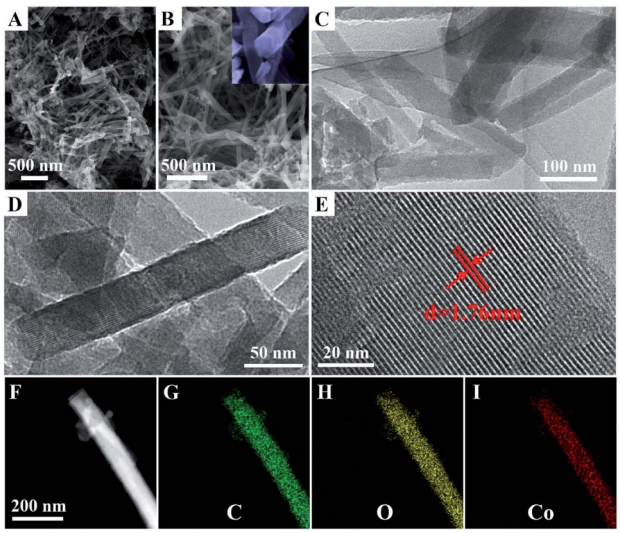

Fig. 1 Morphology and microstructure of Co-CAT MOF. (A) and (B) SEM images, (C) and (D) TEM images, and (E) HRTEM image of Co-CAT MOF. (F) HAADF-STEM image and (G)–(I) the corresponding EDX mapping of C, O and Co elements.

The crystalline phase and surface chemical state of the synthesized Co-CAT MOF are further determined. Fig. 2A compares the measured XRD pattern and the calculated relative diffractions of Co-CAT crystals. The good consistence indicates the phase purity of the sample. The two diffraction peaks centered at 4.65° and 9.34° correspond to the (100) and (200) planes of Co-CAT,[45] respectively, further indicating the stacking of two-dimensional conjugate planes along the *c*-axis.[43,44] The XPS survey spectrum shows that the sample is composed of C, O and Co elements without any other impurities (Fig. S1†), which agrees with the EDX mapping results. Fig. 2B–D show the high-resolution spectra of the different elements. The C 1s spectrum (Fig. 2B) can be divided into peaks with binding energies of 284.1, 284.7, 285.9 and 288.1 eV, assigned to C=C, C–C, C–O, and C=O functional groups, respectively.[41,44,45] The O 1s peak (Fig. 2C) can be well fitted with three components, namely Co–O (531.8 eV), O–C (532.8 eV), and O=C (533.4 eV).[41,44] For the Co 2p spectrum (Fig. 2D), the peaks located at 781.3 eV and 797.3 eV correspond to Co $2p_{3/2}$ and Co $2p_{1/2}$. The appearance of two satellite peaks at 785.7 eV and 802.5 eV suggests that the cobalt element is divalent in Co-CAT MOF.[44] The XPS analyses are consistent with the previous studies.[44,47]

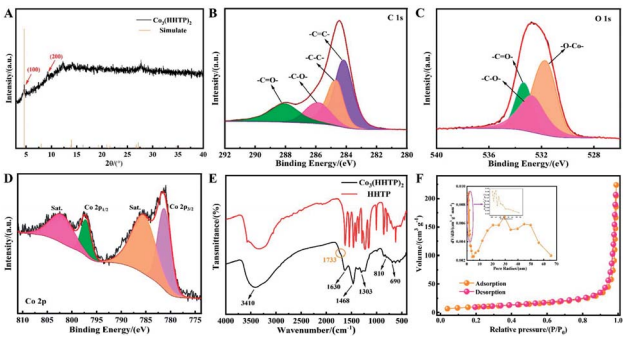

Fig. 2 Spectral analysis and surface properties of Co-CAT MOF. (A) The observed and calculated XRD patterns. High-resolution XPS spectra of (B) C 1s, (C) O 1s, and (D) Co 2p regions. (E) FT-IR spectra for Co-CAT and HHTP. (F) BET surface area and pore size distribution curve (inset) of Co-CAT MOF.

The surface molecular components and structures of the Co-CAT MOF are further identified with FTIR. Fig. 2E gives the infrared absorption spectra of the organic ligand HHTP and Co-CAT MOF. The peaks at 3410 cm^{-1} and 1468 cm^{-1} are attributed to the O–H tensile vibration and the C=C tensile vibration, respectively.[48] The peak at 1630 cm^{-1} is the characteristic absorption band of the benzene ring, and the two absorption peaks at 690 and 810 cm^{-1} represent the out-of-plane C–H bending vibration of the benzene ring building blocks.[49] The results reveal the existence of the benzene ring in Co-CAT MOF. In addition, there is a small peak at 1733 cm^{-1} in Co-CAT MOF, which corresponds to the C=O stretching vibration. Considering the reaction shown in Scheme S1† and the FTIR results, we demonstrate the successful synthesis of Co-CAT MOF. To test the thermal stability, the Co-CAT MOF was heated up to 700 °C with a heating rate of 10 °C min^{-1} in an air atmosphere (Fig. S2†). The TG curve of Co-CAT MOF shows a significant drop in the temperature range of 50–240 °C, which is attributed to the desorption of H_2O molecules and other solvent molecules from the internal pores. Co-CAT MOF was completely decomposed at approximately ~460 °C, and eventually formed cobalt oxides.

Fig. 2F shows the N_2 adsorption/desorption curve of the Co-CAT MOF sample. The specific surface area measured by the Brunauer–Emmett–Teller (BET) method is 49.5 m^2 g^{-1}. This value is much lower than the theoretical specific surface area of typical MOF materials (400–500 m^2 g^{-1}),[43] but it is still comparable with some synthesized MOFs, for example, Co-TDC (22 m^2 g^{-1}),[50] H-Co-MOF (49.9 m^2 g^{-1}),[51] and $Co_3(HHTP)_2$ (61 m^2 g^{-1}).[44] The decreased specific surface area of Co-CAF MOF is due to the large lateral size. Additionally, it should be mentioned here that, for the application of MOF-based electrodes, a higher specific surface area will form a large area of solid electrolyte interphase (SEI) film, resulting in a lower initial coulombic efficiency and poor cycle stability.[52] Therefore, a suitable specific surface area is required for the practical applications. The pore structure of Co-CAT MOF measured by the Barrett–Joyner–Halenda (BJH) method shows main distribution at 3.0–4.0 nm and 40–100 nm (Fig. 2F inset). The micropore formation is due to the inherent hexagonal channels in Co-CAT MOF, while the mesopores are attributed to the gaps between MOF nanowires. The distribution of different kinds of pores in the active material can alleviate the volume change during cycling, and facilitate the electrolyte contact, leading to good cycle stability and high specific capacity for ion storage.

Fig. 3A shows the first five CV curves of the Co-CAT MOF electrode with a scan rate of 0.1 mV s^{-1} within the voltage window of 0.01–3.0 V (*vs.* K^+/K). In the first cathodic scan, a major broad peak appears at 0.49 V, which becomes weak in the subsequent scans. This peak is mainly due to the irreversible side reactions, such as electrolyte decomposition and SEI

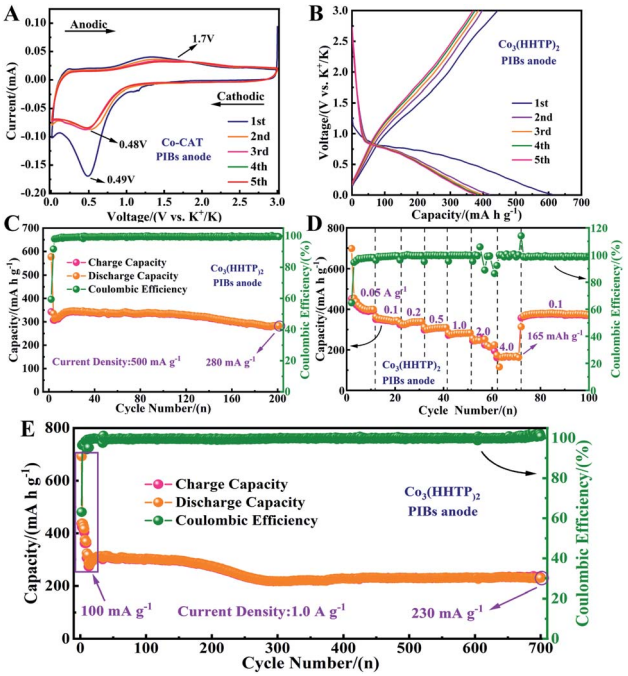

Fig. 3 Electrochemical performance of the Co-CAT MOF electrode for potassium-ion storage: (A) CV profiles of Co-CAT MOF at 0.1 mV s^{-1}. (B) Galvanostatic discharge/charge curves at a current density of 200 mA g^{-1}. Cycle stability tested at a current density of (C) 500 mA g^{-1}. (D) Rate performances of the Co-CAT MOF electrode. (E) Long-term stability tests at a high current density of 1000 mA g^{-1}.

formation on the electrode surface.[10,53] From the second to the fifth cycle, a new reduction peak at 0.48 V appears, which belongs to the gradual embedding of potassium ions in the benzene rings of Co-CAT MOF. With the steady intercalation of potassium ions, charge repulsion increases in the conjugated system, making the reduction peak broad.[49] In the subsequent cycles, the SEI film stabilizes, and the CV curves are highly overlapping. An oxidation peak near 1.7 V was detected during the initial five scans, which corresponds to the reversible extraction of potassium ions. Fig. 3B shows the discharge–charge curves of the first five cycles of the Co-CAT MOF electrode measured at a current density of 200 mA g^{-1}. During the initial discharge process, the open circuit voltage drops sharply to 1.0 V, which is attributed to the pseudocapacitive adsorption effect of the potassium ions, leading to a negligible contribution to the total capacity.[33] When the battery is further discharged to 0.6 V, the potential drops slowly, in accordance with the reversible potassiation process. In the first cycle, the discharge and charge capacities are 602.7 and 390.3 mA h g^{-1}, respectively, and the corresponding coulombic efficiency is 64.8%. The irreversible capacity loss comes from the SEI formation and electrolyte decomposition. In the next cycles, the Co-CAT electrode exhibits a stable reversible specific capacity of 363.3 mA h g^{-1}, with a coulombic efficiency exceeding 98%. Both the CV and discharge–charge results indicate that the Co-CAT MOF electrode has good reversibility and stability for potassium ion storage. The Co-CAT MOF was also tested at a low current density of 100 mA g^{-1}. As shown in Fig. S3,† the electrode possesses a reversible specific capacity of 332 mA h g^{-1} after 80 cycles. Fig. S4† compares the morphology of the electrode before and after the cycling tests. The surface of the fresh electrode is smooth (Fig. S4A†). During the cycling, an SEI film is formed, but the electrode surface is still relatively flat, and the Co-CAT MOF morphology is well maintained (Fig. S4B†). Fig. 3C shows the cycling performance of the Co-CAT MOF electrode tested at a current density of 500 mA g^{-1}. The electrode shows a high reversible specific capacity of 280 mA h g^{-1} after 200 cycles. Except for the initial cycle, the coulombic efficiency is close to 100%, indicating good cycle reversibility.

The active species after 200 cycles are analysed by TEM and SEM to evaluate the structural stability. As shown in Fig. S5,† the Co-CAT MOF still maintains the rod-like morphology after cycling. On the rod surface, there is an overcoat amorphous layer with a thickness of ~10 nm, which is attributed to the formation of the SEI (Fig. S5A†). EDX mapping confirms the uniform distribution of the main elements along the nanorod (Fig. S5B†). The cross-sectional morphology of the fresh electrode is studied by SEM and compared with the electrode after cycling. Before the stability test, the electrode surface (electrolyte side) is relatively rough, and the average thickness is ~9.0 μm (Fig. S6A†). Fig. S6B† indicates that the spatial distribution of carbon, oxygen and cobalt elements is uniform. After 200 cycles tested at 500 mA g^{-1}, the electrode surface is smoother (Fig. S6C†), which is attributed to the formation of the SEI film. The electrode thickness increases to ~10.6 μm. In addition, due to the side reactions such as electrolyte decomposition that occurred on the electrode surface, the electrode shows more abundant carbon and oxygen elements (Fig. S6D†).

Fig. 3D shows the rate performance of the Co-CAT MOF electrode measured under different current densities. When the Co-CAT MOF electrode was tested at current densities of 50, 100, 200, 500, 1000, 2000, and 4000 mA g^{-1}, the specific capacities are 390, 350, 335.5, 310, 280, 240 and 165 mA h g^{-1}, respectively. When the current density returned from 4000 mA g^{-1} to 100 mA g^{-1}, the specific capacity increased to 345 mA h g^{-1}. In order to evaluate the long-term stability under high current density, the Co-CAT MOF electrode was tested at 1 A g^{-1} (Fig. 3E). In the initial 300 cycles, the specific capacity undergoes a sluggish decreasing process, which relates to the activation process of the battery. In the following cycles, the battery cycles stably because of the gradual formation of the SEI film at high current densities.[54–56] After 700 cycles, the electrode delivers a reversible capacity of 230 mA h g^{-1} with a coulombic efficiency of ~100%. The Co-CAT MOF electrode also shows a higher reversible specific capacity than other typical MOF-based anodes for PIBs (Fig. S7 and Table S1†), for example, K_2TP (249 mA h g^{-1} at 200 mA g^{-1}),[57] MOF-235/graphene (180 mA h g^{-1} at 200 mA g^{-1}),[58] MIL-125(Ti) (155 mA h g^{-1} at 50 mA g^{-1})[59] and MOF-235/CNTs (144 mA h g^{-1} at 50 mA g^{-1}).[60]

To understand the origin of the excellent potassium storage performance of the Co-CAT MOF anodes, we used different electrochemical techniques to study the ion storage kinetics during the charge and discharge process. Firstly, the galvanostatic intermittent titration method (GITT) was employed to

calculate the potassium-ion diffusion coefficient D_{K^+}.[61,62] In the initial cycle, galvanostatic discharge/charge was applied for 0.5 h at a current density of 100 mA g^{-1}, and then the coin cell was fully rested for 4 h for relaxing. Based on the GITT test, combined with Fick's second law, the potassium-ion diffusion coefficient can be obtained from the following formula:

$$D_{K^+} = \frac{4}{\pi\tau}\left(\frac{m_B V_m}{M_B S}\right)^2\left(\frac{\Delta E_s}{\Delta E_t}\right)^2\left(\tau \ll \frac{L^2}{D_{K^+}}\right) \quad (1)$$

where m_B, V_m, M_B, S and L are the Co-CAT mass, molar volume, molecular weight, contact area between the electrode and the electrolyte (~0.785 cm^2), and electrode thickness, respectively. ΔE_s and ΔE_t are the voltage changes caused by pulse discharge and constant current discharge respectively (Fig. 4A and D). The variation of the potassium-ion diffusion coefficient with voltage during the first discharge process is shown in Fig. 4B. At the beginning of potassiation, the diffusion coefficient reaches 10^{-11} cm^2 s^{-1}, which is attributed to the K^+ adsorption, and is consistent with the galvanostatic charge/discharge results (Fig. 3B). As potassium ions need a path to reach the active sites, the subsequent diffusion coefficient decreases. Under a low voltage, potassium ions are inserted into the active sites gradually, and the diffusion coefficient remains stable. Fig. 4E shows the changing of potassium-ion diffusion coefficient during the charge process. As the voltage increases, the diffusion coefficient decreases sharply and then remains stable, corresponding to the migration of lithium ions from the active sites of Co-CAT MOF. The calculated high diffusion coefficient (10^{-12} to 10^{-9} cm^2 s^{-1}) is derived from the unique one-dimensional morphology and the intrinsic pore structure of the Co-CAT MOF, which is close to the sulfur-grafted hollow carbon spheres.[15] Furthermore, the Co-CAT MOF electrode shows a linear relationship between voltage (V) and root time ($t^{1/2}$, $s^{1/2}$) in the discharge (Fig. 4C) and charge process (Fig. 4F), demonstrating the accuracy of the calculations.

Fig. 5A shows the CV curves of the Co-CAT MOF electrode obtained at different scan rates ranging from 0.1 to 2.0 mV s^{-1}. With the increase of scan rates, the curve contours are similar, indicating that the Co-CAT electrode shows excellent rate performance and low polarization rate.[63] The peak current values (i, mA) and scan rates (v, mV s^{-1}) have the following relationship:

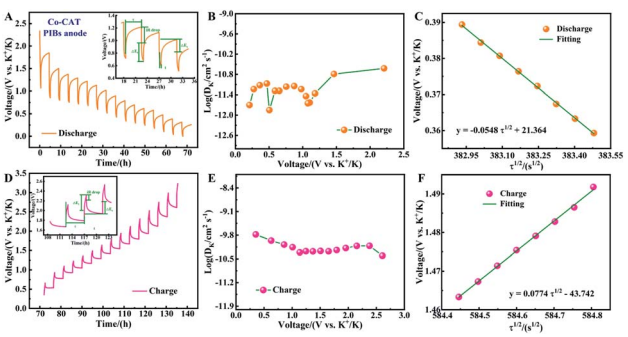

Fig. 4 GITT curves of the Co-CAT MOF electrode for the (A) discharge and (D) charge processes in the initial cycle at 100 mA g^{-1}. The variation of D_{K^+} during (B) discharge and (E) charge processes. The corresponding linear behavior of voltage and $t^{1/2}$ during (C) discharge and (F) charge processes.

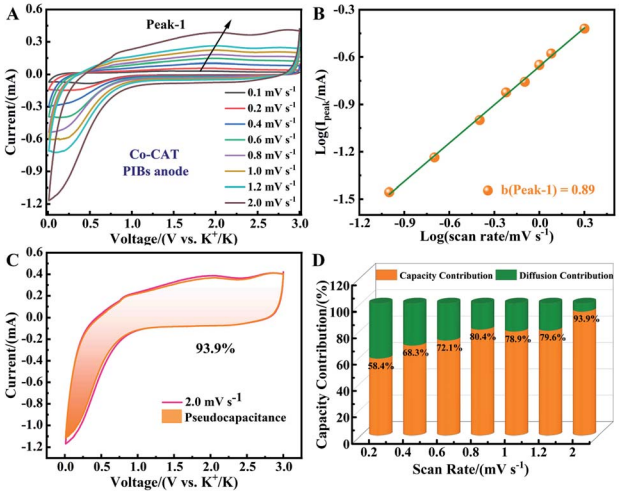

Fig. 5 Pseudocapacitive performance of the Co-CAT MOF electrode for PIBs. (A) CV profiles of the Co-CAT MOF with different scan rates. (B) Correlation between log(I_{peak}, mA) and log(scan rate, mV s^{-1}). (C) Contribution of the pseudocapacitance of the Co-CAT MOF electrode at the scan rate of 2.0 mV s^{-1}. (D) Capacity-/diffusion-contribution ratio of Co-CAT MOF with different scan rates.

$$i = av^b \quad (2)$$

$$\log(i) = b\log(v) + \log(a) \quad (3)$$

where a and b are constants, and the b value can be used to judge the ion storage mechanism, either controlled by diffusion ($b = 0.5$) or by pseudocapacitance ($b = 1.0$).[64,65] From Fig. 5B, the fitted b value using the oxidation peak is 0.89, indicating that the potassiation/depotassiation process is mainly controlled by the pseudocapacitance process.

The pseudocapacitance contribution can be further analyzed using the following formula:

$$i(V) = k_1 v + k_2 v^{1/2} \quad (4)$$

$$i(V)/v^{1/2} = k_1 v^{1/2} + k_2 \quad (5)$$

where $k_1 v$ and $k_2 v^{1/2}$ represent the pseudocapacitance contribution and diffusion control contribution, respectively.[66] As shown in Fig. 5C, the pseudocapacitance contribution is 93.9% at a scan rate of 2.0 mV s^{-1}. The pseudocapacitance contribution gradually increases from 58.4% to 93.9% as the scan rate rises from 0.2 mV s^{-1} to 2.0 mV s^{-1} (Fig. 5D). Hence, the high specific capacity and rate performance of Co-CAT MOF are mainly attributed to the pseudocapacitance effect.

The kinetics parameters were also investigated by measuring the EIS of the Co-CAT MOF electrode. Fig. S8A† presents the EIS profiles of the Co-CAT MOF electrode at different depths of discharge in the initial discharge process. As the potassium ion insertion proceeds, the semicircle diameters in the spectrum

become smaller, indicating that the charge transfer is enhanced.[41,67,68] Especially when it is discharged to 0.5 V, the interface resistance decreases sharply. After discharging to 0.01 V, the interface resistance suddenly increases, which is caused by the SEI formation that hinders the ion transportation. The impedance spectra of electrodes with different cycles (cycle 2 and cycle 12) are shown in Fig. S8B.† The interface resistance of the original electrode is very large, and it decreases with the gradual cycling, showing a rapid charge transfer process and a better cycle performance induced by the electrode activation. The combination of the high potassium-ion diffusion coefficient, pseudocapacitance effect, and stable charge transfer resistance makes the Co-CAT MOF electrode exhibit excellent potassium ion storage performance.[69]

We studied the potassium-ion storage mechanism of the Co-CAT MOF electrode by using various *ex situ* characterization techniques (XPS, FTIR and Raman) to track the surface electronic states and structural evolution during charging and discharging processes, aiming to reveal the essence of the excellent potassium storage performance.

Fig. 6A–C display high-resolution XPS spectra of the C 1s core level of the Co-CAT electrode under different charge and discharge states. The C 1s spectrum of the initial electrode can be divided into four parts, including C=C, C–C, C–O and C=O.[41] When discharged to 0.01 V, the Co-CAT MOF electrode is fully potassiated. The peaks centered at 292.8 eV and 295.6 eV are attributed to the interaction of K^+ with the π-electrons of the benzene ring in Co-CAT MOF (or π–K^+ interaction).[70] In the subsequent depotassiation process, the intensities of these two peaks become weakened noticeably, indicating that most of the potassium ions are separated from the redox sites, but some potassium ions are still retained in the system, which is consistent with the CV and charge/discharge results (Fig. 3A and B). Fig. 6D shows the K 2p spectra. The K $2p_{1/2}$ and K $2p_{3/2}$ peaks are significantly weaker in the fully charged state, compared with the discharged state. This is consistent with the result of the F 1s spectrum (Fig. S9†). Concurrently, the content of C=C decreases and the content of C–C increases in the fully discharged state (Fig. 6B), also suggesting the interaction of K^+ with the aromatic ring. After charging back to 3.0 V, the peaks of C=C and C–C recover reversibly, which induces a high initial coulombic efficiency. Fig. 6E represents the surface electronic state of Co element at different states. In the fresh electrode, the two peaks at 797.3 and 781.4 eV are attributed to Co $2p_{1/2}$ and Co $2p_{3/2}$. While discharging to 0.01 V, the binding energies of Co $2p_{1/2}$ and Co $2p_{3/2}$ shift to 795.6 and 779.8 eV, which is caused by the change in the Co coordination environment. Although the binding energy of Co 2p changes slightly after complete discharging, no obvious change in the energy difference between Co $2p_{1/2}$ and $2p_{3/2}$ is observed, indicating that the Co element preserves the divalent state.[71] When the electrode was charged up to 3.0 V, the Co element still existed in the divalent state. Therefore, the Co central nodes are not active sites for potassium-ion storage.

Fig. 6F shows the *ex situ* FTIR data of Co-CAT MOF in different states in the first cycle. The peak at 700–800 cm^{-1} is attributed to the out-of-plane bending vibration of the aromatic ring, while the peak at ~1181 cm^{-1} is related to the C–C band.[72] During discharging, the peak intensity at 1300–1450 cm^{-1} steadily increases, due to the conversion of unsaturated =C–H to saturated –C–H bonds.[72] The peak intensity becomes weaker after depotassiation, indicating the formation of the =C–H bond again. At the same time, the characteristic peak of C–C bonds at ~1181 cm^{-1} is observed in the potassiated-electrode, which is weakened after charging to 3.0 V and disappears completely, suggesting the insertion of K^+ into the unsaturated C=C on benzene rings, and the result is consistent with XPS analysis.

Fig. 6G shows a series of Raman spectra of the electrode at different states. The D peak (~1330 cm^{-1}) and G peak (~1600 cm^{-1}) represent disordered carbon (such as disordered layers, edges, atomic defects, *etc.*), and in-phase vibration of the graphite lattice. The relative intensity ratio of the D peak to G peak (I_D/I_G) is an indicator for evaluating the amount of disorder or the in-plane crystallite size in the sample. The larger the I_D/I_G value, the more carbon defects.[73] During discharging, the G peak undergoes a blue shift, which can be explained by the charging effect generated by K^+ insertion and SEI formation.[73] In the subsequent charging process, the G peak returned to its original position, which shows that the reaction is reversible. The calculated I_D/I_G value increases as the potential decreases (Fig. 6H) implying an increased structural disorder due to the interaction of K^+ with the benzene ring. In the depotassiation process, the I_D/I_G value drops significantly (Fig. 6I), indicating the reversible reaction of K^+ with sp^2 carbon.

Taking the above independent *ex situ* measurements together, we propose the following potassium-ion storage mechanism for the unit of Co-CAT MOF (Scheme 1).

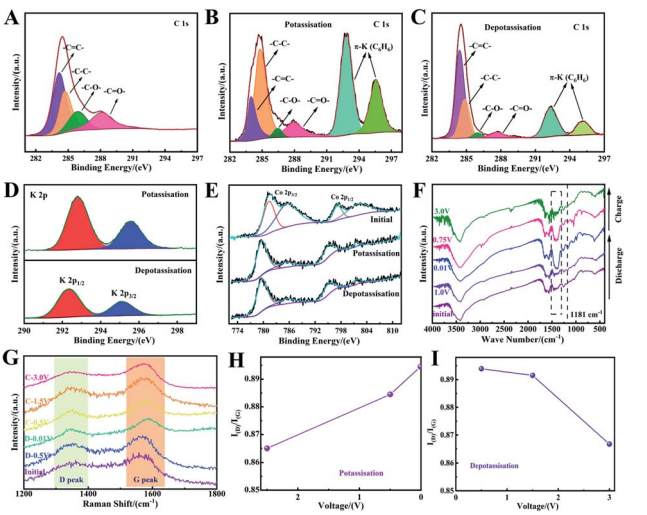

Fig. 6 *Ex situ* XPS spectra of the C 1s core level of the Co-CAT MOF electrode under different charge and discharge states. (A) The fresh electrode, (B) potassiation-electrode, (C) depotassiation-electrode. XPS spectra of (D) K 2p and (E) Co 2p core levels. (F) *Ex situ* FTIR spectra of the Co-CAT MOF electrode in different states. (G) *Ex situ* Raman spectra and corresponding calculated I_D/I_G values at the full (H) potassiation and (I) depotassiation states.

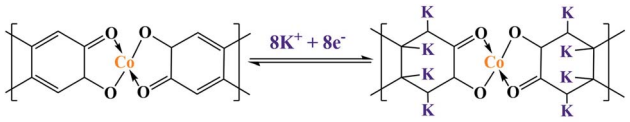

Scheme 1 Schematic illustration of the potassium-ion storage mechanism for the unit of Co-CAT MOF.

As the potential drops, the potassium ion undergoes a redox reaction with the C=C bond in the Co-CAT MOF to form a C–C bond structure; when charging to 3.0 V, the potassium ion gradually escapes from the Co-CAT MOF. During the charge/discharge process, the metal node Co and other structures are electrochemically inactive in the redox reaction.

Based on the above analysis, the theoretical capacity of Co-CAT MOF for potassium ion storage can be calculated:

$$C_{th} = nF/3.6M \quad (6)$$

where n is the number of transferred electrons ($n = 8$), F is the Faraday constant (96 485.33C mol^{-1}), and M is the relative molecular weight of the repeating unit that undergoes the redox reaction.[31] The calculated theoretical capacity C_{th} is 785.4 mA h g^{-1}, yielding the capacity contributed by one potassium ion reaction of 98.2 mA h g^{-1}. Fig. S10† shows the initial discharge profile for Co-CAT MOF measured at a small current density of 25 mA g^{-1}. The first discharge capacity is 786.7 mA h g^{-1}, which is close to the calculated maximum capacity, further confirming the proposed 8-electron redox mechanism.

Accordingly, the excellent electrochemical performance of the Co-CAT MOF electrode is due to the following factors. (1) The abundant redox sites in Co-CAT MOF are involved in potassium ion storage, whereas the nanostructure facilitates sufficient electrolyte infiltration, improves active site utilization and increases K^+ storage capacity. (2) The planar conjugated structure of Co-CAT MOF promotes charge transfer, and the three-dimensional nanostructure contributes to rapid electron/ion transfer and enhances the rate performance of Co-CAT MOF. (3) The nanostructure can alleviate the volume change during cycling and the unique redox reaction mechanism maintains the stability of the electrode structure, and these factors endow the Co-CAT MOF with excellent cycling stability.

Thanks to the excellent structural characteristics, we expect that the Co-CAT MOF electrode can also show good performance for lithium storage. In light of this, coin cells were assembled for electrochemical tests. The CV curves of Co-CAT MOF are shown in Fig. 7A. The CV curves were tested at a scan rate of 0.1 mV s^{-1} in the voltage window 0.01–3.0 V. The appearance of a broad reduction peak at ~0.88 V in the first cathodic scan and disappearance in subsequent cycles can be attributed to the irreversible side reactions, including electrolyte decomposition, and SEI formation during the initial lithiation, analogous to the potassiation reaction.[41,44] In the following scans, the Co-CAT MOF electrode undergoes two-step lithiation/delithiation, identified by two pairs of redox

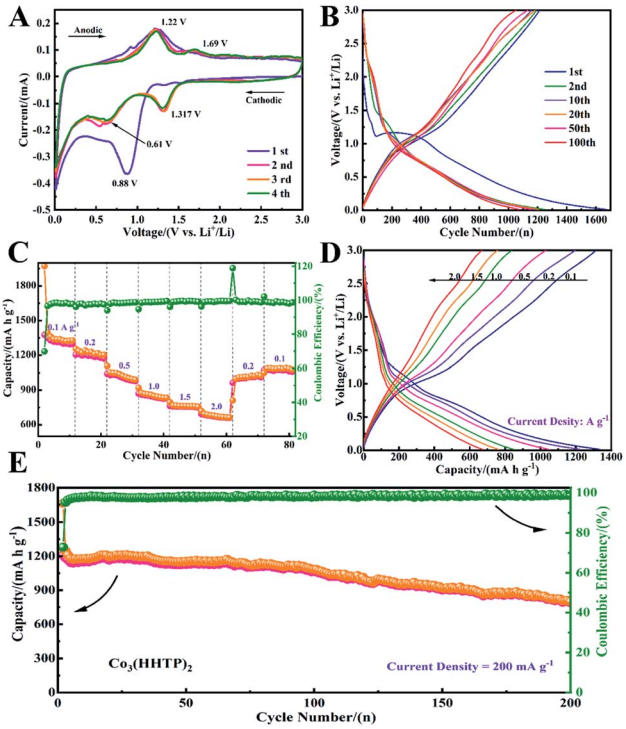

Fig. 7 Electrochemical lithium storage performance of Co-CAT MOF: (A) CV curves of Co-CAT MOF at 0.1 mV s^{-1} (0.01–3.0 V). (B) Discharge–charge plots for different cycles at 200 mA g^{-1}. (C) Rate performance of Co-CAT MOF. (D) Discharge–charge profiles of Co-CAT MOF at different current densities. (E) Cycle performance at a current density of 200 mA g^{-1}.

characteristic peaks at 0.61, 1.22, 1.32, and 1.69 V. Fig. 7B shows the representative discharge–charge curves of the Co-CAT MOF electrode at a current density of 200 mA g^{-1}. In the initial cycle, the discharge and charge specific capacities are 1213.6 and 1671.7 mA h g^{-1}, and the corresponding coulombic efficiency is 72.6%. The irreversible capacity loss comes from the side reactions as discussed above. Fig. 7C displays the rate performance of the Co-CAT MOF. The electrode delivers specific capacities of 1315.1, 1197.5, 1033, 840.6, 785.6 and 669.3 mA h g^{-1} at current densities of 100, 200, 500, 1000, 1500, and 2000 mA g^{-1}. When the current density decreases to 200 mA g^{-1}, the specific capacity increases to 1000 mA h g^{-1}. The galvanostatic discharge–charge curves at different current densities are shown in Fig. 7D. The long-term stability was studied by measuring the Co-CAT MOF electrode at a current density of 200 mA g^{-1} for 200 cycles (Fig. 7E). After the cycling, the electrode still has a reversible specific capacity of 800 mA h g^{-1}. SEM characterization (Fig. S11†) shows that the cycled electrode retains a continuous and complete structure, confirming that the Co-CAT MOF electrode possesses good morphology stability, which is also demonstrated by different *ex situ* tests (see the discussion below). In addition, at a high current density of 5 A g^{-1}, the Co-CAT MOF electrode exhibits a reversible specific capacity of 140 mA h g^{-1} (Fig. S12†). Compared to other Co-based MOF anodes, the Co-CAT MOF electrode delivers a higher reversible specific capacity (Table

S2†), for example, Co-ZIF-67 (122 mA h g^{-1} at 100 mA g^{-1} after 100 cycles),[74] Co-btca (801.3 mA h g^{-1} at 200 mA g^{-1} after 50 cycles),[75] $[Co_2(pztc)(H_2O)_6]_n$ (815 mA h g^{-1} at 200 mA g^{-1} after 150 cycles),[76] and S-$Co_2(OH)_2$BDC (601 mA h g^{-1} at 500 mA g^{-1} after 700 cycles).[77]

The CV curves obtained with different scan rates (Fig. S13A†) are used to reveal the charge storage mechanism of Co-CAT MOF. The *b* values (see eqn (2) and (3)) are calculated as shown in Fig. S13B.† The fitted *b* values at the three redox peaks are 0.878 (peak 1), 0.745 (peak 2) and 0.976 (peak 3), respectively, indicating that the lithiation process is controlled by diffusion and capacitive processes together.[63,66] Furthermore, using the above method, the calculated pseudocapacitance contribution reaches 80% at a scan rate of 1.0 mV s^{-1} (Fig. S13C†), and it gradually increases from 59.0% to 92.8% as the scan rate increases from 0.2 to 2.0 mV s^{-1} (Fig. S13D†). From GITT results, lithium-ion diffusion coefficients ranging from 10^{-9} to 10^{-10} cm^2 s^{-1} are derived (Fig. S14†). The diffusion coefficient of lithium-ion in the Co-CAT MOF electrode is slightly higher than that of potassium-ion. This may be due to the fact that the radius of lithium ion (0.076 nm) is smaller than that of potassium ion (0.138 nm), and lithium ion exhibits stronger diffusivity.[5] The conductive MOF structure and one-dimensional morphology of Co-CAT are responsible for the fast ion transportation. EIS of the Co-CAT electrode before cycling and after 1 and 10 cycles are shown in Fig. S15.† The radius of the semicircular area decreases, indicating that the reaction kinetics gradually accelerates.

Ex situ characterization is used to study the lithium storage of Co-CAT MOF (Fig. S16†). Fig. S16A–C† show high-resolution C 1s XPS spectra of the fresh electrode, lithiated electrode and delithiated electrode. A new peak appears at 289.7 eV during discharging, which is attributed to the C–Li formation, indicating the reaction between lithium ions with the benzene ring.[78] As shown in Fig. S16D,† in the original electrode, the two peaks at 797.3 eV and 781.4 eV are attributed to Co $2p_{1/2}$ and Co $2p_{3/2}$. When discharged to 0.01 V, the binding energies of Co $2p_{1/2}$ and Co $2p_{3/2}$ shift to 797.1 eV and 781.2 eV, which is caused by the coordination environment change during discharging. The Co element remains in the divalent state since there is no change in the binding energy difference between Co $2p_{1/2}$ and $2p_{3/2}$. And the valence of Co is still +2 when charged to 3.0 V. It means the Co central nodes are inactive for lithium storage.[71] According to FTIR analysis (Fig. S16E†), a new absorption peak appears near 1639 cm^{-1} when discharged to 0.5 V (point B). This peak gradually increases as the discharge process continues (points B and C), and it still appears even at the end of the charging, which is related to the irreversible reactions. The change of FTIR spectra in the range of 1750–1680 cm^{-1} is negligible, indicating the electrochemical inertness of the C=O functional group.[72] From XRD results (Fig. S16F†), the phase structure of Co-CAT MOF is stable at the different charge/discharge states. No obvious peak shift is observed, suggesting that the interplanar spacing of the diffraction planes remains constant. It further demonstrates the good stability of Co-CAT MOF for the lithium storage.

Due to the smaller radius of lithium ion (0.076 nm) and the mesoporous pore size distribution of Co-CAT MOF (Fig. 2F inset), the inner pores also serve as effective ion storage centers, leading to a higher lithium storage capacity than that contributed by the 8-electron redox involving the benzene ring unit (785.4 mA h g^{-1}). Therefore, different from the potassium-ion storage, the potential active sites for lithium-ion storage include both benzene ring and inner pores (Fig. S16G†). Such a lithium storage mechanism is like that of Cu-CAT MOF, which has the same structure as that of the Co-CAT MOF.

Due to the high specific capacity and excellent rate performance of the Co-CAT anode, a full cell was assembled to verify the practical feasibility (Fig. 8). Commercial $LiCoO_2$ was selected as the cathode, and the capacity matching principle was used to assemble the full cell. CV was used to test the half-cell made by the $LiCoO_2$ cathode and $Co_3(HHTP)_2$ anode, respectively, and then a specific voltage range of 0.5–4.2 V voltage was selected to test the full cell electrochemical performance.[33,41] Fig. 8B shows the cycle stability of the Co-CAT//$LiCoO_2$ full cell at a current density of 200 mA g^{-1}. The full cell shows good stability after the initial capacity decay. After 100 cycles, the reversible specific capacity remains 404 mA h g^{-1}. The performance is better than that of the $Cu_3(HHTP)_2$//$LiNi_{0.8}Co_{0.1}Mn_{0.1}O_2$ (Cu-CAT//NCM811) full cell with a similar configuration,[41] which shows a capacity of 371 mA h g^{-1} after 200 cycles at the same current density. Fig. 8C shows the charge–discharge curves of the Co-CAT//$LiCoO_2$ full cell at different current densities ranging from 0.1 to 2.0 A g^{-1}. The Co-CAT//$LiCoO_2$ full cell can release a specific capacity of 546.1 mA h g^{-1} even at a high current density of 2 A g^{-1}. Fig. 8D shows the rate performance of the full cell, which exhibits specific capacities of 890.4, 847.7, 745.2, 649.2, 892.2 and 546.1 mA h g^{-1} at current densities of 0.1, 0.2, 0.5, 1.0, 1.5 and 2.0 A g^{-1}, respectively. When the current density returns to

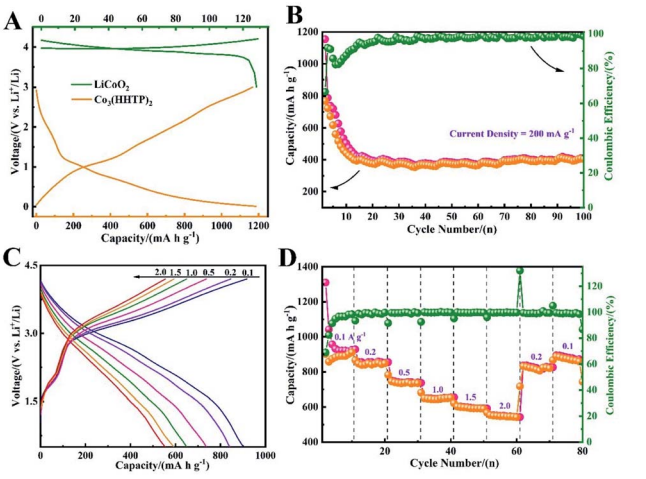

Fig. 8 Electrochemical performance of the Co-CAT//$LiCoO_2$ full cell: (A) galvanostatic charge–discharge curves of Co-CAT and $LiCoO_2$ with the voltage window of 0.5–4.2 V (200 mA g^{-1}). (B) Cycling stability test of the Co-CAT//$LiCoO_2$ full cell at 200 mA g^{-1}. (C) Charge–discharge profiles at different current densities. (D) Rate performance of the Co-CAT//$LiCoO_2$ full cell.

0.2 A g^{-1}, the specific capacity of the full cell increases to 820.1 mA h g^{-1} again, showing excellent reversible stability performance. The results confirm the feasibility of the Co-CAT MOF anode for practical applications.

Conclusions

In summary, we have successfully synthesized nanostructured Co-CAT MOF using a simple liquid-phase method. When used as the anode for PIBs, the Co-CAT MOF shows excellent potassium storage performance. In particular, the electrode provides a reversible capacity of 332 mA h g^{-1} at 0.1 A g^{-1}. At a high current density of 4.0 A g^{-1}, it also exhibits a capacity of 165 mA h g^{-1}. Long term stability measurements indicate that the Co-CAT MOF electrode maintains a capacity of 230 mA h g^{-1} at the current density of 1.0 A g^{-1} after 700 cycles. The measured potassium storage performance is superior to the results reported so far. The excellent electrochemical performance of the Co-CAT MOF anode is attributed to the conductive nature of the MOF structure, which facilitates charge transfer and electrolyte infiltration, and mitigates the volume change during cycling. Combining kinetic analysis and *ex situ* characterization, we proposed that the potassium storage in the Co-CAT MOF is through an 8-electron transfer process. In addition, the Co-CAT MOF also shows good lithium storage performance both with half-cell and full-cell configurations. The Co-CAT MOF delivers a reversible capacity of 800 mA h g^{-1} after 200 cycles at the current density of 200 mA g^{-1}. The Co-CAT//$LiCoO_2$ full cell shows a capacity of 404 mA h g^{-1} at 200 mA g^{-1} after 100 cycles. This work demonstrates the potential of c-MOF anodes for potassium/lithium storage applications, and the proposed potassium/lithium-ion storage mechanism can be employed to design and synthesize other novel electrode materials for energy storage. We also note here that by choosing cheap and suitable organic ligands during the synthesis, it is possible to upscale the electrode production for potential industrial applications.

Conflicts of interest

There are no conflicts to declare.

Acknowledgements

This study was financially supported by the National Natural Science Foundation of China (52177208, 52171202, 51971055, 51871046). We also thank Dr Ningyan Cheng and Ms Siqi Guo of the Institutes of Physical Science and Information Technology (Anhui University) for help with the TEM characterizations.

Notes and references

1 J. Li, Y. Cai, H. Wu, Z. Yu, X. Yan, Q. Zhang, T. Z. Gao, K. Liu, X. Jia and Z. Bao, *Adv. Energy Mater.*, 2021, **11**, 2003239.
2 P. Zhai, K. Liu, Z. Wang, L. Shi and S. Yuan, *J. Power Sources*, 2021, **499**, 229973.
3 K. Liu, C. Li, L. Yan, M. Fan, Y. Wu, X. Meng and T. Ma, *J. Mater. Chem. A*, 2021, **9**, 27234–27251.
4 X. Zhang, J. Chen, Z. Xu, Q. Dong, H. Ao, Z. Hou and Y. Qian, *Energy Storage Mater.*, 2022, **46**, 147–154.
5 X. Kuai, K. Li, J. Chen, H. Wang, J. Yao, C.-L. Chiang, T. Liu, H. Ye, J. Zhao and Y.-G. Lin, *ACS Nano*, 2022, **16**(1), 1502–1510.
6 L. Fan, Q. Liu, S. Chen, K. Lin, Z. Xu and B. Lu, *Small*, 2017, **13**, 1701011.
7 K. Song, C. Liu, L. Mi, S. Chou, W. Chen and C. Shen, *Small*, 2021, **17**, 1903194.
8 R. Rajagopalan, Y. Tang, X. Ji, C. Jia and H. Wang, *Adv. Funct. Mater.*, 2020, **30**, 1909486.
9 X. Wu, Y. Chen, Z. Xing, C. W. K. Lam, S.-S. Pang, W. Zhang and Z. Ju, *Adv. Energy Mater.*, 2019, **9**, 1900343.
10 J. Ge, L. Fan, J. Wang, Q. Zhang, Z. Liu, E. Zhang, Q. Liu, X. Yu and B. Lu, *Adv. Energy Mater.*, 2018, **8**, 1801477.
11 K. Share, A. P. Cohn, R. Carter, B. Rogers and C. L. Pint, *ACS Nano*, 2016, **10**, 9738–9744.
12 P. Xiao, S. Li, C. Yu, Y. Wang and Y. Xu, *ACS Nano*, 2020, **14**, 10210–10218.
13 Y. Sun, H. Wang, W. Wei, Y. Zheng, L. Tao, Y. Wang, M. Huang, J. Shi, Z.-C. Shi and D. Mitlin, *ACS Nano*, 2020, **15**, 1652–1665.
14 Y. Dong, Z.-S. Wu, S. Zheng, X. Wang, J. Qin, S. Wang, X. Shi and X. Bao, *ACS Nano*, 2017, **11**, 4792–4800.
15 J. Ding, H. Zhang, H. Zhou, J. Feng, X. Zheng, C. Zhong, E. Paek, W. Hu and D. Mitlin, *Adv. Mater.*, 2019, **31**, 1900429.
16 Z. Tai, Q. Zhang, Y. Liu, H. Liu and S. Dou, *Carbon*, 2017, **123**, 54–61.
17 Q. Huang, X. Fan, X. Ou, H. Wang, L. Wu and C. Yang, *J. Colloid Interface Sci.*, 2021, **604**, 157–167.
18 F. Wang, Y. Liu, H.-J. Wei, T.-F. Li, X.-H. Xiong, S.-Z. Wei, F.-Z. Ren and A. A. Volinsky, *Rare Met.*, 2021, **40**, 448–470.
19 S. Chen, Y. Feng, J. Wang, E. Zhang, X. Yu and B. Lu, *Sci. China Mater.*, 2021, **64**, 547–556.
20 R. Hu, K. Zhu, K. Ye, J. Yan, Q. Wang, D. Cao and G. Wang, *Appl. Surf. Sci.*, 2021, **536**, 147832.
21 C. Zhao, H. Chen, H. Liu, L. Yin, Q. Zhang, S. Yu, P. Liu, G. Zhong, C.-Z. Lu and Y. Yang, *J. Mater. Chem. A*, 2021, **9**, 6274–6283.
22 P. Lian, Y. Dong, Z.-S. Wu, S. Zheng, X. Wang, S. Wang, C. Sun, J. Qin, X. Shi and X. Bao, *Nano Energy*, 2017, **40**, 1–8.
23 Z. Hong, H. Maleki, T. Ludwig, Y. Zhen, M. Wilhelm, D. Lee, K.-H. Kim and S. Mathur, *J. Energy Chem.*, 2021, **62**, 660–691.
24 W. Zhang, W. Huang and Q. Zhang, *Chem.–Eur. J.*, 2021, **27**, 6131–6144.
25 X. Liu and Z. Ye, *Adv. Energy Mater.*, 2021, **11**, 2003281.
26 C. Li, K. Wang, J. Li and Q. Zhang, *Nanoscale*, 2020, **12**, 7870–7874.
27 J. Lin, R. C. K. Reddy, C. Zeng, X. Lin, A. Zeb and C.-Y. Su, *Coord. Chem. Rev.*, 2021, **446**, 214118.
28 A. Tang, X. He, H. Yin, Y. Li, Y. Zhang, S. Huang and D. G. Truhlar, *J. Phys. Chem. C*, 2021, **125**, 9679–9687.
29 C. Li, X. Hu and B. Hu, *Electrochim. Acta*, 2017, **253**, 439–444.
30 R. Zhao, Z. Liang, R. Zou and Q. Xu, *Joule*, 2018, **2**, 2235–2259.
31 S. Gu, Z. Bai, S. Majumder, B. Huang and G. Chen, *J. Power Sources*, 2019, **429**, 22–29.

32 L. S. Xie, G. Skorupskii and M. Dincă, *Chem. Rev.*, 2020, **120**, 8536–8580.
33 A. Nazir, H. T. Le, A.-G. Nguyen and C.-J. Park, *Electrochim. Acta*, 2021, 138750.
34 H. Meng, Y. Han, C. Zhou, Q. Jiang, X. Shi, C. Zhan and R. Zhang, *Small Methods*, 2020, **4**, 2000396.
35 X.-W. Liu, T.-J. Sun, J.-L. Hu and S.-D. Wang, *J. Mater. Chem. A*, 2016, **4**, 3584–3616.
36 Y.-F. Wang, S.-Y. Yang, Y. Yue and S.-W. Bian, *J. Alloys Compd.*, 2020, **835**, 155238.
37 K. Qi, R. Hou, S. Zaman, Y. Qiu, B. Y. Xia and H. Duan, *ACS Appl. Mater. Interfaces*, 2018, **10**, 18021–18028.
38 P. Mao, G. Lan, C. Liu, Z. Wang, Y. Liu, H. Sun and W. Huang, *Sustainable Mater. Technol.*, 2021, **30**, e00354.
39 Z. Wu, D. Adekoya, X. Huang, M. J. Kiefel, J. Xie, W. Xu, Q. Zhang, D. Zhu and S. Zhang, *ACS Nano*, 2020, **14**, 12016–12026.
40 C.-J. Yao, Z. Wu, J. Xie, F. Yu, W. Guo, Z. J. Xu, D.-S. Li, S. Zhang and Q. Zhang, *ChemSusChem*, 2020, **13**, 2457–2463.
41 L. Guo, J. Sun, W. Zhang, L. Hou, L. Liang, Y. Liu and C. Yuan, *ChemSusChem*, 2019, **12**, 5051–5058.
42 W. Zhu, A. Li, Z. Wang, J. Yang and Y. Xu, *Small*, 2021, **17**, 2006424.
43 M. Hmadeh, Z. Lu, Z. Liu, F. Gándara, H. Furukawa, S. Wan, V. Augustyn, R. Chang, L. Liao, F. Zhou, E. Perre, V. Ozolins, K. Suenaga, X. Duan, B. Dunn, Y. Yamamto, O. Terasaki and O. M. Yaghi, *Chem. Mater.*, 2012, **24**, 3511–3513.
44 J. Sun, L. Guo, X. Sun, J. Zhang, Y. Liu, L. Hou and C. Yuan, *J. Mater. Chem. A*, 2019, **7**, 24788–24791.
45 W. Xiong, X. Cheng, T. Wang, Y. Luo, J. Feng, S. Lu, A. M. Asiri, W. Li, Z. Jiang and X. Sun, *Nano Res.*, 2020, **13**, 1008–1012.
46 D. Xing, Y. Wang, P. Zhou, Y. Liu, Z. Wang, P. Wang, Z. Zheng, H. Cheng, Y. Dai and B. Huang, *Appl. Catal., B*, 2020, **278**, 119295.
47 H. Yoon, S. Lee, S. Oh, H. Park, S. Choi and M. Oh, *Small*, 2019, **15**, 1805232.
48 R. S. Kumar, S. S. Kumar and M. A. Kulandainathan, *Microporous Mesoporous Mater.*, 2013, **168**, 57–64.
49 S. Maiti, A. Pramanik, U. Manju and S. Mahanty, *Microporous Mesoporous Mater.*, 2016, **226**, 353–359.
50 Y. Ning, X. Lou, M. Shen and B. Hu, *Mater. Lett.*, 2017, **197**, 245–248.
51 L. Chen, W. Yang, J. Wang, C. Chen and M. Wei, *Chem.–Eur. J.*, 2018, **24**, 13362–13367.
52 J. Wang, L. Liao, H. R. Lee, F. Shi, W. Huang, J. Zhao, A. Pei, J. Tang, X. Zheng and W. Chen, *Nano Energy*, 2019, **61**, 404–410.
53 J. Yang, Z. Ju, Y. Jiang, Z. Xing, B. Xi, J. Feng and S. Xiong, *Adv. Mater.*, 2018, **30**, 1700104.
54 C. Li, C. Zhang, J. Xie, K. Wang, J. Li and Q. Zhang, *Chem. Eng. J.*, 2021, **404**, 126463.
55 H. Jiang, Z. Wei, L. Ma, Y. Yuan, J. J. Hong, X. Wu, D. P. Leonard, J. Holoubek, J. J. Razink, W. F. Stickle, F. Du, T. Wu, J. Lu and X. Ji, *Angew. Chem., Int. Ed.*, 2019, **58**, 5286–5291.
56 A. Li, B. Qian, M. Zhong, Y. Liu, Z. Chang and X.-H. Bu, *Mater. Chem. Front.*, 2019, **3**, 1398–1405.
57 K. Lei, F. Li, C. Mu, J. Wang, Q. Zhao, C. Chen and J. Chen, *Energy Environ. Sci.*, 2017, **10**, 552–557.
58 Q. Deng, Z. Luo, H. Liu, Y. Zhou, C. Zhou, R. Yang, L. Wang, Y. Yan and Y. Xu, *Ionics*, 2020, **26**, 5565–5573.
59 Y. An, H. Fei, Z. Zhang, L. Ci, S. Xiong and J. Feng, *Chem. Commun.*, 2017, **53**, 8360–8363.
60 Q. Deng, S. Feng, P. Hui, H. Chen, C. Tian, R. Yang and Y. Xu, *J. Alloys Compd.*, 2020, **830**, 154714.
61 Y. Zhu and C. Wang, *J. Phys. Chem. C*, 2010, **114**, 2830–2841.
62 H. Zhang, P. Zong, M. Chen, H. Jin, Y. Bai, S. Li, F. Ma, H. Xu and K. Lian, *ACS Nano*, 2019, **13**, 3054–3062.
63 C. An, Y. Yuan, B. Zhang, L. Tang, B. Xiao, Z. He, J. Zheng and J. Lu, *Adv. Energy Mater.*, 2019, **9**, 1900356.
64 Z. Wei, P. Mao, C. Liu, G. Lan, M. Ahmad, R. Zheng, Z. Wang, H. Sun and Y. Liu, *ACS Appl. Mater. Interfaces*, 2021, **13**, 58652–58664.
65 H. Fan, P. Mao, G. Lan, C. Liu, J. Chen, Z. Wang, Z. Li, R. Zheng, Y. Liu and H. Sun, *ACS Appl. Energy Mater.*, 2021, **4**, 9440–9449.
66 X.-B. Zhong, F. Gao, C. He, P. Radjenovic, Z.-Q. Tian and J.-F. Li, *J. Phys. Chem. C*, 2020, **124**, 10845–10851.
67 S. Yang, Y. Huang, G. Han, J. Liu and Y. Cao, *Powder Technol.*, 2017, **322**, 84–91.
68 Y. Luo, R. Guo, T. Li, F. Li, L. Meng, Z. Yang, Y. Wan and H. Luo, *ChemElectroChem*, 2019, **6**, 690–699.
69 M. Tang, Y. Wu, Y. Chen, C. Jiang, S. Zhu, S. Zhuo and C. Wang, *J. Mater. Chem. A*, 2019, **7**, 486–492.
70 X. Chen, H. Zhang, C. Ci, W. Sun and Y. Wang, *ACS Nano*, 2019, **13**, 3600–3607.
71 Y. Liu, X. Zhao, C. Fang, Z. Ye, Y.-B. He, D. Lei, J. Yang, Y. Zhang, Y. Li and Q. Liu, *Chem*, 2018, **4**, 2463–2478.
72 X. Han, G. Qing, J. Sun and T. Sun, *Angew. Chem., Int. Ed.*, 2012, **51**, 5147–5151.
73 M. Shimizu, T. Koya, A. Nakahigashi, N. Urakami, T. Yamakami and S. Arai, *J. Phys. Chem. C*, 2020, **124**, 13008–13016.
74 H. Wang, Y. Bai, X. Jiang and M. Zeng, *Appl. Surf. Sci.*, 2021, **546**, 149119.
75 Y. Luo, L. Sun, F. Xu, S. Wei, Q. Wang, H. Peng and C. Chen, *J. Mater. Sci. Technol.*, 2018, **34**, 1412–1418.
76 J. Liu, L. Zhang, H. Li, P. Zhao, P. Ren, W. Shi and P. Cheng, *Sci. China: Chem.*, 2019, **62**, 602–608.
77 C. Li, X. Hu, X. Lou, L. Zhang, Y. Wang, J.-P. Amoureux, M. Shen, Q. Chen and B. Hu, *J. Mater. Chem. A*, 2016, **4**, 16245–16251.
78 C. Xu, B. Sun, T. Gustafsson, K. Edström, D. Brandell and M. Hahlin, *J. Mater. Chem. A*, 2014, **2**, 7256–7264.

